STRUCTURAL BIOLOGY

ISSN 2059-7983

Cryo-EM reveals how omecamtiv mecarbil readies myosin for phosphate release

Sean N. McMillan,[a,b,c] Donald A. Winkelmann,[d] Stephen P. Muench[b,c] and Charlotte A. Scarff[a,b]*

[a]Discovery and Translational Science Department, Leeds Institute of Cardiovascular and Metabolic Medicine, School of Medicine, Faculty of Health and Life Sciences, University of Leeds, Leeds, United Kingdom, [b]Astbury Centre for Structural Molecular Biology, University of Leeds, Leeds, United Kingdom, [c]School of Biomedical Sciences, Faculty of Health and Life Sciences, University of Leeds, Leeds, United Kingdom, and [d]Department of Pathology and Laboratory Medicine, Robert Wood Johnson Medical School, Rutgers University, Piscataway, NJ 08854, USA. *Correspondence e-mail: c.a.scarff@leeds.ac.uk

Received 19 June 2026
Accepted 11 November 2026

Edited by T. Burnley, Rutherford Appleton Laboratory, United Kingdom

This article is part of the Proceedings of the 2025 CCP-EM Spring Symposium.

Keywords: β-cardiac myosin; myosin modulators; omecamtiv mecarbil; cardiac activator.

EMDB references: myosin·OM, EMD-58408; myosin·ADP·P_i, EMD-58409

PDB references: myosin·OM, 31gy; myosin·ADP·P_i, 31gz

Supporting information: this article has supporting information at journals.iucr.org/d

Omecamtiv mecarbil (OM) was considered to be a cardiac muscle activator in clinical trials for alleviation of systolic heart failure. Yet, it was later shown to be a potent inhibitor of myosin motor activity. Its binding to myosin prevents the force-generating lever swing but also accelerates the release of inorganic phosphate (P_i), such that in muscle OM enhances overall force production by cooperatively increasing the number of actomyosin cross-bridges. The structural basis by which it accelerates P_i release remains poorly understood. Here, using cryogenic electron microscopy, we determined the structure of the human β-cardiac myosin motor domain in the presence of MgATP and OM to 3.2 Å global resolution. The structure adopts a primed state with well resolved OM density within its established binding pocket, and density within the active site consistent with a post-hydrolysis MgADP·P_i state. OM stabilizes interactions bridging the converter and N-terminal subdomains of the myosin motor, inducing a 11° lever rotation and altering relay-helix conformation relative to the drug-free motor to prevent the force-generating lever swing. Comparison of this structure with that of bovine cardiac myosin with OM and MgADP·vanadate bound, determined by crystallography, revealed subtle but meaningful differences. OM remodels the nucleotide-binding site, shifting the P_i density ∼2 Å towards its proposed exit pathway. This altered P_i coordination provides a plausible structural rationale for a mechanism by which OM accelerates the weak-to-strong actomyosin-binding transition, key to its therapeutic function. By stabilizing a conformation in which P_i is not coordinated to MgADP, P_i is likely freely released upon opening of its exit pathway. This structural observation is also consistent with previous kinetic studies that showed that OM shifts the equilibrium constant for ATP hydrolysis towards the post-hydrolysis state. This mechanistic understanding will be beneficial to the development of more effective myosin-targeting therapeutics.

1. Introduction

Development of small molecules to directly modulate myosin is a rapidly growing therapeutic avenue, promising treatments for both hyper- and hypo-contractile heart diseases and heart failure, all significant global health problems (Amr *et al.*, 2024; Day *et al.*, 2022; Ali *et al.*, 2021). Omecamtiv mecarbil (OM) was the first myosin modulator to be identified as a potential treatment for systolic heart failure (Morgan *et al.*, 2010). Yet, despite multiple completed and ongoing phase III clinical trials (Teerlink *et al.*, 2021; Lewis *et al.*, 2022), OM has yet to gain FDA approval. A more complete understanding of its mechanism of action may nevertheless inform future clinical development and the design of next-generation myosin-targeting therapeutics.

In the heart, myosin generates contractions through the work of many myosin motors in consort, each applying

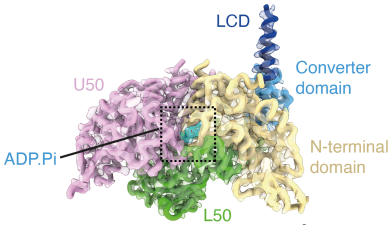

OPEN ACCESS
Published under a CC BY 4.0 licence

mechanical force to actin filaments leading to muscle shortening (Huxley, 1969; Geeves & Holmes, 1999). The force-generation process is referred to as the myosin chemomechanical cycle and describes the conformational transitions that the myosin motor undergoes to generate force, fuelled by chemical energy from ATP hydrolysis, and controlled by the nucleotide- and actin-binding state (Robert-Paganin *et al.*, 2020).

Upon binding ATP, myosin is released from actin, and undergoes a recovery stroke, where the lever moves from a 'down' to an 'up' position, followed by ATP hydrolysis. In its ADP·P_i (primed) state myosin associates with actin, initially weakly, primarily through the helix–loop–helix of its lower 50 kDa subdomain (L50), and then strongly, as actin promotes the weak-to-strong binding transition associated with actin-binding cleft closure and binding of the upper 50 kDa subdomain (U50) hypertrophic cardiomyopathy loop to actin. This is closely followed by a force-generating lever swing termed the powerstroke or working stroke (Klebl *et al.*, 2025). Whether P_i is released before or after lever swing has been hotly debated (Debold, 2021; Robert-Paganin *et al.*, 2020).

Structural studies show that P_i must be released from the active site to enable actin-binding cleft closure (Klebl *et al.*, 2025), yet it is not observed in solution until much later (Muretta *et al.*, 2015), on a timescale in which lever swing would have already occurred. The unified theory is thus that P_i exits the active site prior to lever swing, on the microsecond timescale, but then resides with the myosin motor, in an area termed the P_i release tunnel, for hundreds of milliseconds before being released into solution (Woody *et al.*, 2019; Moretto *et al.*, 2022). Following lever swing, ADP is released, associated with a smaller change in lever position, and then ATP re-binds to recommence the cycle.

Detailed understanding of this myosin chemomechanical cycle is needed to understand how it may be altered by disease and how these alterations may be remedied by small-molecule therapies such as OM. Early characterization of OM showed it increased the ATPase activity of cardiac myosin (Morgan *et al.*, 2010) and that this was due to the compound accelerating actin-activated P_i release (Nagy *et al.*, 2015; Malik *et al.*, 2011). However, single-molecule studies showed that despite accelerating P_i release, OM inhibited the force-generating lever swing (Woody *et al.*, 2018).

The binding site for OM was subsequently identified in a crystal structure of bovine cardiac myosin in complex with OM and ADP·VO_4 (Auguin *et al.*, 2024; Planelles-Herrero *et al.*, 2017), showing how the compound interacted with the primed motor conformation between the converter domain and N-terminal domain, acting as a molecular glue to prohibit lever swing (Auguin *et al.*, 2024; Planelles-Herrero *et al.*, 2017). Together, these studies showed that OM was a myosin inhibitor but activated muscle through cooperatively increasing the lifetime of actomyosin cross-bridges, prolonging systolic contraction (Woody *et al.*, 2018).

However, the crystal structure was unable to provide a structural rationale for why the compound accelerates P_i release or shifts the equilibrium constant for ATP hydrolysis as it was obtained in the presence of the P_i analogue VO_4, which mimics an ATP-hydrolysis intermediate and acts as a strong inhibitor of myosin ATPase activity (Wilson *et al.*, 1995; Goodno, 1979, 1982). Understanding the full mechanism of action of OM is key to its effective use and for the further development of myosin-targeting therapeutics. Thus, we investigated the structure of cardiac myosin in complex with OM and in the presence of the native MgATP substrate to reveal how the compound affects P_i handling.

2. Methods

2.1. Expression and purification of *β*-cardiac heavy meromyosin

The human cardiac heavy meromyosin (cHMM) used in these studies was produced using an adenovirus–mammalian system as previously described (McMillan *et al.*, 2026)

2.2. cHMM cross-linking

Prior to cryoEM grid preparation cHMM was first prepared by cross-linking with bis(sulfosuccinimidyl)suberate (BS3) for 30 min at 25°C under the following conditions: 2 µ*M* cHMM, ±50 µ*M* OM (5% DMSO), 1 m*M* BS3, 1 m*M* EGTA, 1 m*M* ATP, 2 m*M* $MgCl_2$, 50 m*M* KCl, 10 m*M* MOPS pH 7.2 in a 30 µl reaction volume. To allow for motor priming and compound binding the reaction mixture was incubated at room temperature for 15 min prior to the addition of 1 m*M* BS3. The reaction was then quenched with a 100 m*M* final concentration of Tris pH 8, preventing further cross-linking.

2.3. Cryo-EM grid preparation and data collection

Grids for the motor domain in complex with OM (M·OM), and in the absence of OM (M·ADP·P_i), were prepared using methods optimized to exclude interacting head-motif particles on a Vitrobot Mark IV (Thermo Fisher; McMillan *et al.*, 2026). 3 µl of the BS3 cross-linked cHMM diluted twofold was applied onto an UltrAuFoil R 1.2/1.3 300 mesh gold grid (Quantifoil) glow-discharged for 30 s at 10 mA prior to use (PELCO easiGlow). Grids were blotted with Whatman No. 42 Ashless filter paper (Agar Scientific, UK) for 1–3 s with a force of 6 and a wait time of 2 s at 8°C and 95% humidity before vitrification in liquid ethane.

Data were collected on a FEI Titan Krios (Astbury Biostructure Laboratory, University of Leeds) operating at 300 kV equipped with a Falcon 4 direct electron camera with a specimen pixel size of 0.82 Å. Micrographs were collected using the *EPU* acquisition software at 96 000× with a total dose of ∼43 e^- Å^2 and a defocus range of −1.2 to −3.0 µm. Total collected micrographs were 19 737 over two sessions for M·OM and 19 072 over two sessions for M·ADP·P_i (including the original data from McMillan *et al.*, 2026; Supplementary Figs. S1 and S2 and Table S1).

2.4. CryoEM data processing and model building

Image processing was carried out in *cryoSPARC* v4.51 (Supplementary Fig. S1; Punjani *et al.*, 2017). Raw movies were imported for motion correction and CTF estimation using *cryoSPARC Live* and suboptimal micrographs were removed, leaving a total of 17 347 and 16 157 micrographs for M·OM and M·ADP·P_i, respectively. Accepted micrographs were then denoised using *cryoSPARC* micrograph denoiser and picking was performed using *cryoSPARC* blob picker. Particles were extracted in a box size of 360 × 360 pixels centred on individual motor domains and classified using *cryoSPARC* reference-free 2D classification (Punjani *et al.*, 2017). Classes resembling single motor domains were selected for an additional round of 2D classification before generating an initial model using *cryoSPARC*'s *ab initio* reconstruction into five classes. The resulting maps were then refined using heterogeneous refinement and classes resembling a single motor domain were pooled. Pooled particles were then further refined through homogeneous and non-uniform refinement (Punjani *et al.*, 2017, 2020). One round of reference-based motion correction was performed using the relevant map from non-uniform refinement (Punjani *et al.*, 2017, 2020). Corrected particles were then pooled, resulting in 120 496 and 97 282 particles for M·OM and M·ADP·P_i, respectively. To further remove poor particles new initial models were then obtained using *cryoSPARC*'s *ab initio* reconstruction into five classes followed by heterogeneous refinement. Finally, good classes were once again pooled and refined using homogeneous and non-uniform refinement (Punjani *et al.*, 2017, 2020). The final reconstruction particle number was 96 062 and 72 262 for M·OM and M·ADP·P_i, respectively, with most cHMM particles only contributing one motor domain to that final reconstruction, likely due to variance in particle quality. The resulting maps were then sharpened using a negative *B* factor automatically determined by *cryoSPARC* and local resolution estimation was calculated in *cryoSPARC* (Punjani *et al.*, 2017).

To interpret the motor-domain cryoEM electron-density maps, PDB entry 9gz3 was flexibly fitted into both maps with *ISOLDE* (Croll, 2018). OM was then fitted to the identified density in the M·OM map with *ISOLDE* (Croll, 2018). *Phenix* real-space refinement was then performed followed by adjustments in *Coot* and *ISOLDE*, and was repeated until satisfied (Supplementary Table S2; Emsley *et al.*, 2010; Croll, 2018; Liebschner *et al.*, 2019).

Interpretation, analysis and comparisons of maps and models was performed in *Chimera X* (Pettersen *et al.*, 2021). Lever displacement angle was measured using the *Chimera* measurement tool as the angle between two axes.

2.5. CryoEM 3D classification

In an attempt to resolve the dynamics/heterogeneity of the inorganic phosphate within the active site of the M·OM structure, extensive 3D classification was performed in both *cryoSPARC* and *RELION*. In *cryoSPARC* both global and focused classification (masking the region around the inorganic phosphate; Supplementary Fig. S5) were performed on the particle stack contributing to the final M·OM reconstruction. Classification was performed into five classes, forcing hard classification and with use of latent mixing coefficients to improve separation of low-population subtle density changes. Several filter resolutions between 3 and 5 Å were trialled, with all displaying highly similar results (Supplementary Fig. S5).

For classification in *RELION*, particles contributing to the final M·OM reconstruction were converted to a compatible `.STAR` file format using *pyem*. Once again both local and focused classification (masking the region around the inorganic phosphate; Supplementary Fig. S5) were performed. Classification was performed into five classes without alignment to aid in separation of subtle structural changes. *T* values of up to 10 were assessed to attempt to observe small deviations in high-frequency features, with all showing similar results (Supplementary Fig. S5).

In both *cryoSPARC* and *RELION*, 3D classification failed to adequately separate out any meaningful structural states, with the majority of the particles contributing to a single class despite attempting extensive optimization. To ensure that the highest populated class represented the consensus reconstruction, non-uniform refinement and 3D refinement were performed in *cryoSPARC* and *RELION*, respectively (Supplementary Fig. S5).

3. Results

3.1. CryoEM reconstruction of the myosin motor domain in complex with omecamtiv mecarbil, ADP and P_i

To observe the effects of OM on the β-cardiac heavy meromyosin (cHMM) motor structure in the presence of the native MgATP substrate we solved the complex (M·OM) using cryoEM (Supplementary Fig. S1 and Table S1). Individual β-cardiac myosin motor domains were averaged, and the resulting motor-domain reconstruction was resolved to a global resolution of 3.2 Å. The motor domain was observed to be in a primed conformation with additional defined density for OM (local resolution of ∼3.1 Å) in its previously identified binding site (Figs. 1*a*, 1*b* and 2; Auguin *et al.*, 2024; Planelles-Herrero *et al.*, 2017) and density within the active site consistent with a post-hydrolysis MgADP·P_i state.

To stabilize the full-length cHMM construct, containing the complete 42-heptad S2 region and lacking a stabilizing leucine zipper used in other studies, we cross-linked it with the amine-reactive cross-linker BS3 prior to cryoEM analysis. Whilst chemical cross-linking could, in principle, affect the conformational states sampled by the motor, BS3 possesses a relatively long and flexible spacer arm, allowing substantial positional freedom between linked residues and reducing the likelihood that a particular structural state is enforced. Consistent with this, no density attributable to BS3 was visible in the final reconstruction, nor in previous structures generated using the same cross-linking strategy (McMillan *et al.*, 2026). This suggests that the observed conformations are unlikely to be dictated by the cross-linker and are representative of the underlying structural states of the complex.

Nevertheless, we cannot exclude an effect of BS3 cross-linking on the populations or kinetics of conformational states. Both samples were prepared using the same cross-linking protocol, reducing but not eliminating this potential source of bias.

OM has previously been shown to destabilize the auto-inhibited off-state of myosin termed the interacting-heads motif (IHM). Nevertheless, because inclusion of IHM particles could influence the resulting reconstruction, sample preparation and vitrification methods were optimized to favour isolated motor domains, in a disordered relaxed state, and minimize particles in an IHM conformation (McMillan *et al.*, 2026). Consistent with this, 2D classification did not reveal classes exhibiting an IHM morphology, and no particle populations consistent with an IHM arrangement were seen during subsequent image processing. These observations suggest that IHM particles, if present, constitute a minor fraction of the dataset and are unlikely to contribute significantly to the final reconstruction. In addition, most cHMM particles included within the final reconstruction were found to have contributed only one of their two motor domains to the final reconstruction.

To facilitate data interpretation, a pseudo-atomic model was built by flexibly fitting a primed drug-free motor-domain structure (PDB entry 9gz3) and docking OM by molecular-dynamics driven modelling (Supplementary Table S2; Croll, 2018). This revealed that bound OM bridges contacts between the converter domain and N-terminal domain (NTD) through hydrogen bonding with the backbone of Arg712 and Asn711 on the converter as well as Asp168 on the NTD. This is then supported by an aliphatic network of Arg712, Ile713, Tyr722,

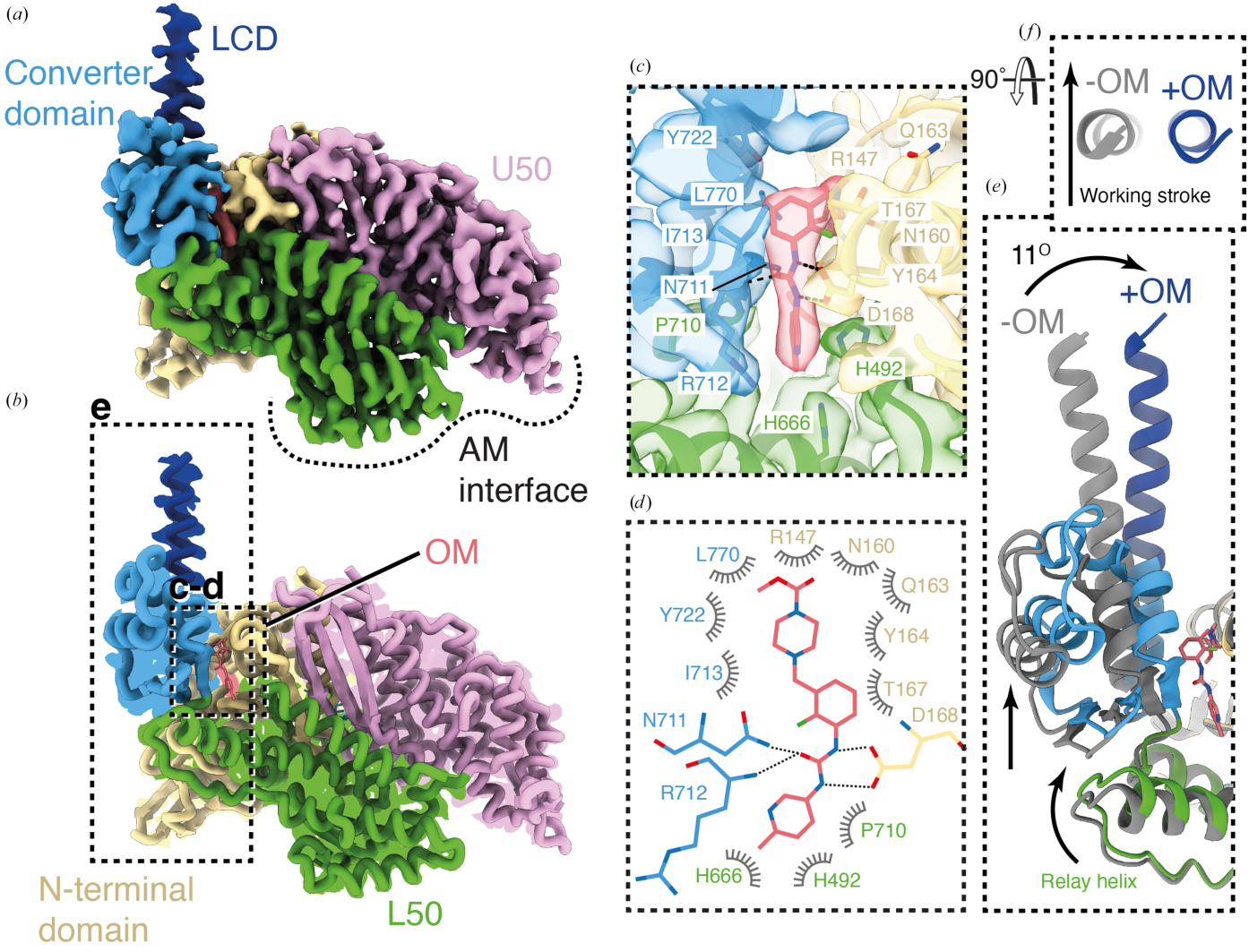

Figure 1
CryoEM reconstruction of myosin motor-domain omecamtiv mecarbil complex. (*a*) Segmented cryoEM map of the β-cardiac myosin motor in complex with OM (contour 0.1), split by subdomain: N-terminal domain, yellow; L50, green; U50, pink; converter domain, light blue; LCD, dark blue; OM, coral; the actomyosin (AM) interface is labelled. Together, the LCD and converter form the lever. (*b*) Pseudo-atomic model, docked into the map, highlighting the OM-binding site and coloured by subdomain as in (*a*). The regions shown in (*c*) and (*d*) and in (*e*) are boxed and labelled **c**-**d** and **e**, respectively. (*c*) Enlarged view of the OM-binding site highlighting interacting residues. (*d*) 2D representation of the OM-binding site. (*e*) Comparison of the β-cardiac myosin motor in complex with OM (+OM; M·OM; coloured) and in its absence (−OM; grey) focusing on relative change in lever (11° shift in lever position seen between two structures) and relay-helix conformation. (*f*) 90° rotation of (*e*) showing the view down the lever helix, highlighting the direction of the working stroke.

Arg721 and Leu770 on the converter domain, Arg147, Asn160, Glu163, Tyr164 and Thr167 on the NTD and His492, His666 and Pro710 on the L50 (Figs. 1*c* and 1*d*).

To examine the specific effects of OM binding we obtained a cryoEM reconstruction of a primed motor, under the same experimental conditions but in the absence of drug (M·ADP·P_i), to an equivalent global resolution (3.1 Å) for comparison (Supplementary Tables S1 and S2 and Fig. S2; see Section 2). This showed that binding of OM rotates the light-chain binding domain (LCD) 11° towards the U50, perpendicular to the myosin working stroke, and alters the relay-helix conformation (Figs. 1*e* and 1*f*).

The cryoEM-determined OM-bound primed human cardiac myosin structure (M·OM) was highly similar to the bovine myosin crystal structure (PDB entry 8qyu; global r.m.s.d. across 746 C^{α} atom pairs = 0.961 Å); however, there were minor differences that are important (Figs. 2*a* and 2*b*; Auguin *et al.*, 2024). The crystal structure captures a change in lever and relay conformation (Auguin *et al.*, 2024), similar to our observations, but the lever is pulled a further 3° closer to the U50 in the cryoEM structure. This is likely permitted within the cryoEM structure by the lack of crystal contacts, as the end of the lever helix (amino acids ∼800–810) and the essential light chain (not modelled) form interactions with the adjacent asymmetric units within the crystal lattice (Figs. 2*c* and 2*d*; Auguin *et al.*, 2024). Likewise, the binding conformation of OM is consistent with that seen for PDB entry 8qyu (Figs. 2*e* and 2*f*); however, in contrast to contact between OM and Lys146 on the NTD seen in PDB entry 8qyu, the cryoEM map shows that Lys146 adopts a different rotamer position facing away from the OM-binding site (Fig. 2*g*). The most substantial change between the two structures, however, is seen in the nucleotide-binding site.

3.2. Omecamtiv mecarbil alters inorganic phosphate coordination

In the drug-free state, clear density attributable to Mg·ADP·P_i is observed within the EM density map. Yet, in the presence of OM, density for P_i, coordinated to density for MgADP, is not seen (Figs. 3*a*–3*c*). Instead, additional density is observed, albeit substantially weaker, adjacent to Ser180. The local resolution at the active site is 2.8–3 Å, and the shift in density, which we have attributed to P_i, is supported by differential density in the corresponding EM density maps (Supplementary Fig. S3). The weaker density, assigned to P_i, may also reflect increased positional heterogeneity within the active site. Extensive 3D classification was performed in both *cryoSPARC* and *RELION* in an attempt to observe the putative P_i dynamics but was unfortunately unsuccessful (see Section 2).

Modelling positions the P_i ∼2 Å away from the P_i position in the drug-free structure (Fig. 3*d*), such that P_i is no longer coordinated with the magnesium ion and instead interacts with Arg243 and Ser241 (Figs. 3*e* and 3*f*). This is of critical importance to understanding the effects of OM on P_i release and ATP hydrolysis.

P_i release occurs when myosin undergoes cleft closure, during which the back door, a salt bridge between Arg243 and Glu466, is broken allowing P_i to exit into the P_i release tunnel. In the OM-bound model we observe that the geometry of the backdoor residues Arg243 and Glu466 is altered, in comparison to the drug-free model, increasing their separation and weakening hydrogen-bond interactions. The shortest interaction distance between backdoor residues (Arg243 NH1 to Glu466 OE2) is increased from 2.6 to 3.1 Å and an interaction between Arg243 and Glu466 is lost (Arg243 NH2 to Gly466 OE1) (Figs. 3*b* and 3*c*).

If the weak density is correctly attributed to P_i, its displacement from MgADP towards the proposed exit pathway, and destabilization of the back door, in the presence of OM would likely prime the motor for P_i release. As the P_i now interacts directly with Arg243 and Ser241 on switch-1 (Fig. 3*f* and Supplementary Fig. S4), as switch-1 moves away from switch-2 upon initiation of cleft closure, exit of P_i into the P_i release tunnel would be more strongly promoted, providing a plausible structural rationale for the reported acceleration of actin-activated P_i release by OM. However, in the absence of actin activation to promote cleft closure, the cleft remains open and P_i remains in the active site.

The observed conformation is also consistent with previous kinetic studies, which showed that in the presence of OM the ATP-hydrolysis equilibrium was significantly biased towards post-hydrolysis without a corresponding increase in maximum hydrolysis (Liu *et al.*, 2015).

This observation could not have been seen in the previous crystal structure as *ortho*-vanadate, an inhibitory analogue, rather than inorganic phosphate is present (Supplementary Fig. S4; Auguin *et al.*, 2024; Planelles-Herrero *et al.*, 2017).

4. Discussion

In this work, we present the cryoEM structure of the cardiac myosin motor domain in complex with OM and MgADP and P_i, uncovering how OM changes nucleotide coordination to accelerate P_i release. We observed that OM affects P_i coordination within the active site, shifting the P_i towards the back door, priming it for release.

This observation aligns with previous experiments investigating the effect of alternate metal ions on myosin kinetics. Replacement of magnesium with manganese was observed to result in a shift of P_i away from the ADP and an increased actin-activated P_i release rate (Ge *et al.*, 2017).

Crucially, this insight was only observable with the use of native MgATP substrate and is absent in previous crystal structures containing the VO_4 phosphate analogue (Auguin *et al.*, 2024; Planelles-Herrero *et al.*, 2017). This is likely due to VO_4 imperfectly mimicking the ATP-hydrolysis intermediate rather than a true ADP·P_i state (Smith & Rayment, 1996; Houdusse *et al.*, 2000). Additionally, VO_4 is a strong inhibitor of myosin activity, forming a stable complex with the myosin motor and ADP (Wilson *et al.*, 1995; Goodno, 1979, 1982) and thus obscuring the subtle allosteric effect of OM. This highlights the importance of using the correct ligands when

investigating the structural effects of activators or inhibitors on their targets.

This work also sheds light on the mechanism of P_i release from the active site into the P_i release tunnel. Here, P_i becomes uncoordinated from magnesium and instead interacts with switch-1 residues (Ser241, Arg243), such that as switch-1 moves away from switch-2 during actin-binding cleft closure, P_i likely moves with it to enter the P_i release tunnel. This is consistent with a previous modelling study, which proposed that P_i can reside at a second site, interacting with Ser180 and Arg243, after release from Mg·ADP (Moretto *et al.*, 2022) and with molecular-dynamics-based investigations

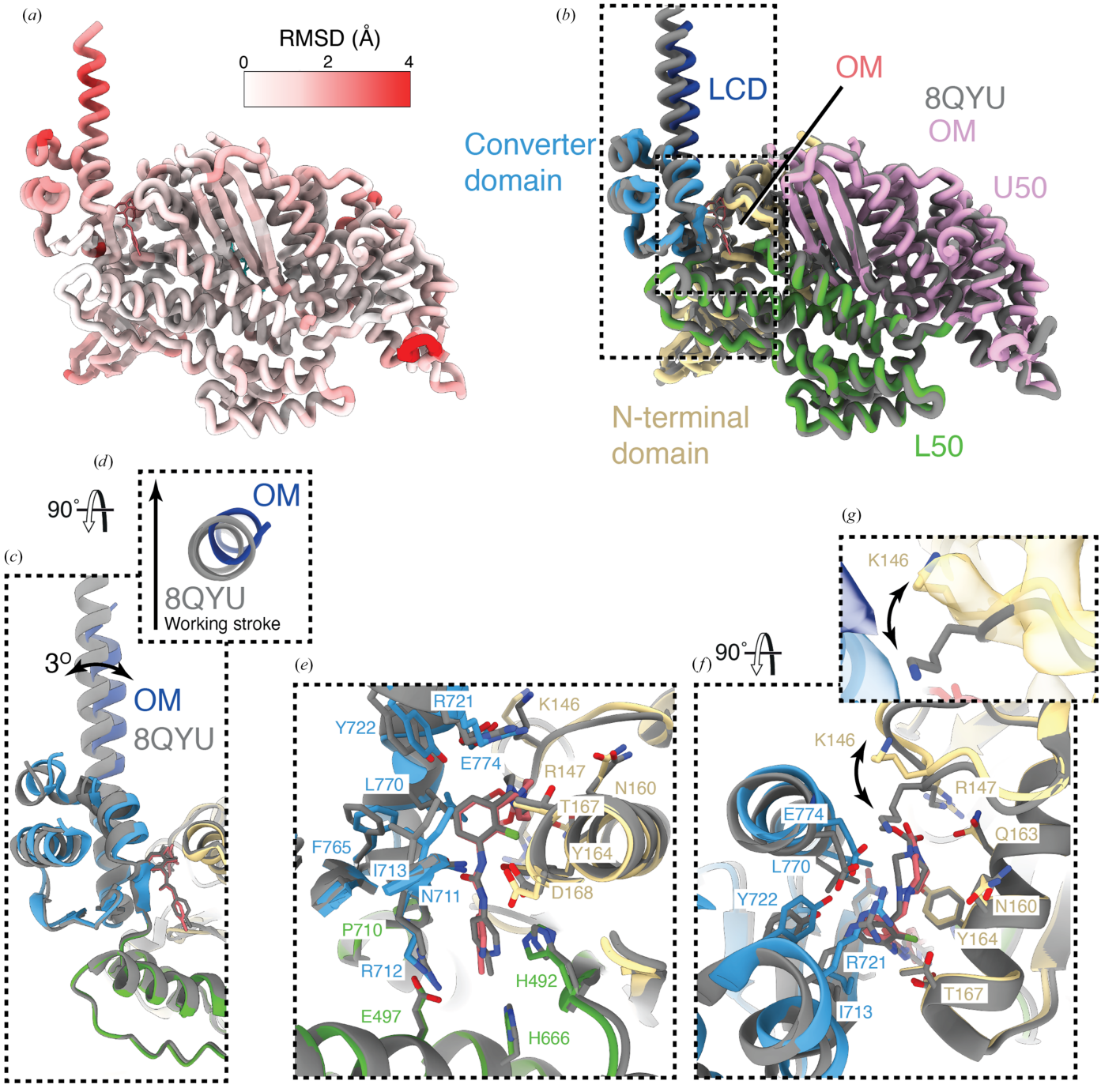

Figure 2
Comparison of cryoEM and crystallographic β-cardiac myosin motor-domain OM complexes. R.m.s.d. comparison of M·OM and PDB entry 8qyu globally aligned coloured on the M·OM model. (*b*) Overlay of M·OM coloured by subdomain [N-terminal domain (NTD), yellow; L50, green; U50, pink; converter domain, light blue; LCD, dark blue; OM, coral] and PDB entry 8qyu (grey). (*c*) Comparison of M·OM (+OM) and lever conformation highlighting the 3° shift coloured as in (*b*). (*d*) 90° rotation of (*c*) showing the view down the lever helix, highlighting the direction of the working stroke. (*e*) Overlay of the OM-binding site compared with PDB entry 8qyu, coloured as in (*b*), highlighting the surrounding residues. (*f*) 90° rotation of (*e*). (*g*) Focused view on change in Lys146 between M·OM and PDB entry 8qyu structures showing the M·OM segmented cryoEM map (contour 0.1) coloured as in (*b*).

proposing exit pathways for P_i from myosin (Cecchini *et al.*, 2010).

Critically, this observation provides structural insight for the increased weak-to-strong actomyosin transition rate in the presence of OM that could not be previously explained. Whilst weak actin binding promotes the actin-binding cleft to close, P_i needs to leave the active site for the cleft to fully close, give strong binding and enable effective force production (Klebl

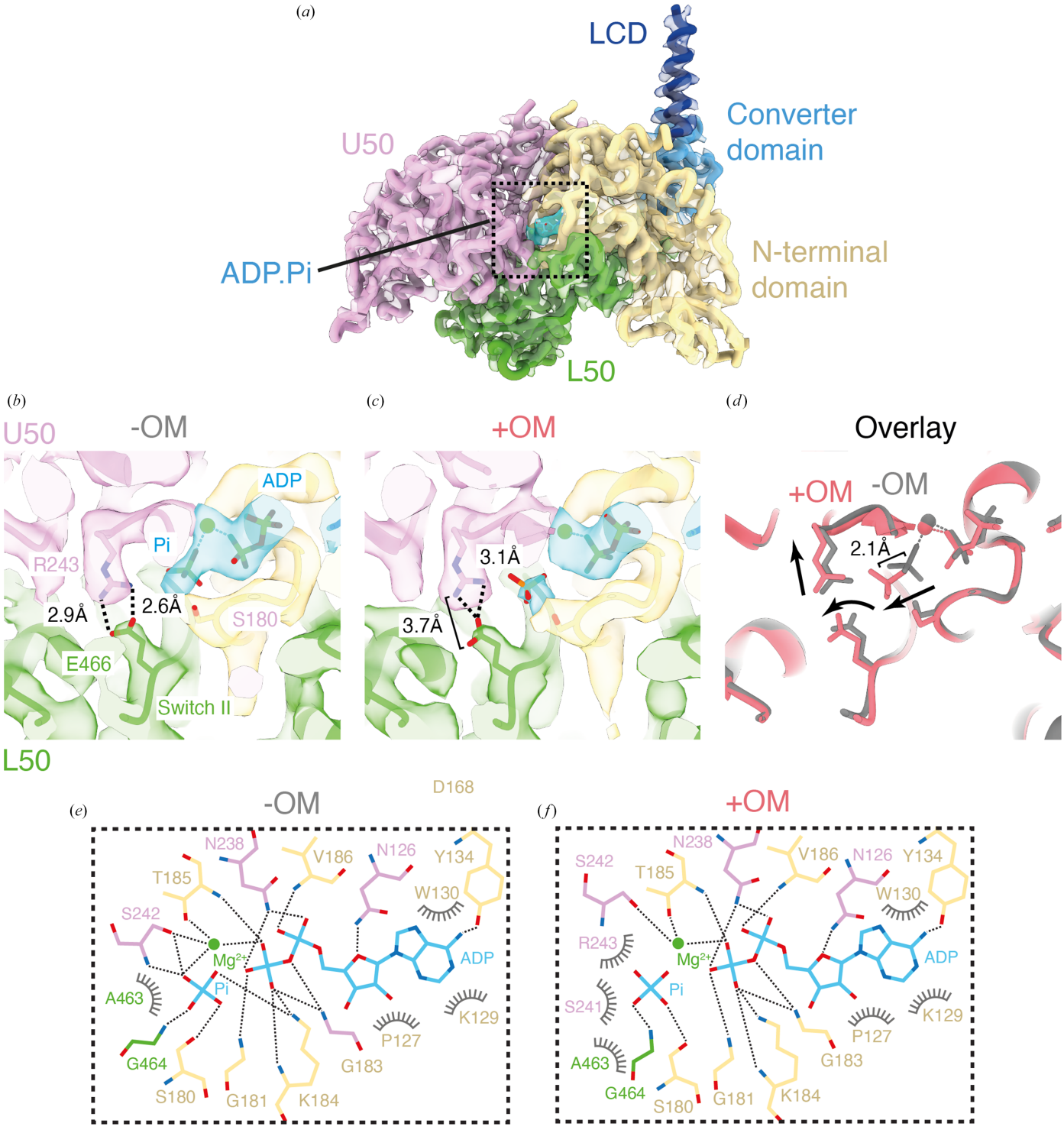

Figure 3
Omecamtiv mecarbil alters inorganic phosphate coordination. (*a*) Pseudo-atomic model coloured by subdomain highlighting the nucleotide site. (*b*, *c*) Segmented cryoEM map of the *β*-cardiac myosin motor nucleotide-binding site coloured as in Fig. 1(*a*), highlighting MgADP·P_i and the interaction distance between backdoor residues Arg243 and Glu466 as well as Ser180 that interacts with the P_i in (*b*) M·ADP·P_i and (*c*) M·OM (+OM). (*d*) Overlay of M·ADP·P_i (grey) and OM complex (yellow) models highlighting the shift in both backdoor residues Arg243 and Glu466 as well as the 2.1 Å change in P_i position. (*e*, *f*) 2D representation of active-site interactions in (*e*) M·ADP·P_i and (*f*) M.OM

et al., 2025). Thus, the priming of P_i for release is likely what greatly accelerates actin-activated cleft closure and thus the weak-to-strong actomyosin transition in the presence of OM.

Whilst this work suggests how OM accelerates actin-activated P_i release there are still unknowns in its mechanism of action. Actin detachment of myosin in the presence of OM is assumed to be noncanonical as it has been shown to be ATP-independent. Actin attachment is prolonged in the presence of OM, and the powerstroke is eliminated (Woody *et al.*, 2018). This means that in the presence of OM, myosin release from actin must happen when OM is still bound, or the OM-bound actomyosin structure must be perturbed in such a way that OM dissociation does not allow the powerstroke to occur. A structure of the OM-bound actomyosin state is thus needed to understand the full mechanism of drug action, and this may be obtainable using time-resolved cryoEM methods such as those used to determine the primed actomyosin complex (Klebl *et al.*, 2025).

Acknowledgements

We thank the members of the cryoEM community at Leeds for their help and guidance. All EM data were collected at the Astbury Biostructure facility funded by the University of Leeds (UoL ABSL award) and Wellcome (108466/Z/15/Z and 221524/Z/20/Z). Author contributions were as follow. CAS designed the project. DAW produced the β-cardiac myosin. SNM performed the cryoEM grid preparation, screening, optimization and data collection. SNM performed the cryoEM data processing, model building and validation. SNM, CAS, DAW and SPM performed cryoEM data analysis and interpretation. SNM performed main figure and supplementary figure generation. SNM and CAS wrote the manuscript. All authors discussed the results and commented on the manuscript.

Conflict of interest

There are no conflicts of interest.

Data availability

The electron-density maps and atomic models for M·OM and M·ADP·P_i have been deposited in the EMDB and PDB with accession codes EMD-58408 and EMD-58409 and 31gy and 31gz, respectively. The following map/model was used for comparison purposes in the study: bovine S1 cardiac myosin in complex with ADP·VO_4 and OM, PDB entry 8qyu.

Funding information

This work was supported by a British Heart Foundation Jacqueline Murray Coomber Fellowship (FS/0/21/34704), a Royal Society research grant (RGS\R1\231276) and MRC project grant (UKRI581) awarded to CAS and an NIH grant (5R01HL157997) to DAW. SNM was supported by a School of Molecular and Cellular Biology, University of Leeds, funded PhD studentship and a BBSRC Project Grant (UKRI1958) awarded to SPM.

References

Ali, A., Abdelmaseih, R., Thakker, R., Faluk, M. & Hasan, S. M. (2021). *Heart Views*, **22**, 275–279.
Amr, A., Kayvanpour, E., Reich, C., Koelemen, J., Asokan, S., Frey, N., Meder, B. & Sedaghat-Hamedani, F. (2024). *Rev. Cardiovasc. Med.* **25**, 225.
Auguin, D., Robert-Paganin, J., Réty, S., Kikuti, C., David, A., Theumer, G., Schmidt, A. W., Knölker, H.-J. & Houdusse, A. (2024). *Nat. Commun.* **15**, 4885.
Cecchini, M., Alexeev, Y. & Karplus, M. (2010). *Structure*, **18**, 458–470.
Croll, T. I. (2018). *Acta Cryst.* D**74**, 519–530.
Day, S. M., Tardiff, J. C. & Ostap, E. M. (2022). *J. Clin. Invest.* **132**, e148557.
Debold, E. P. (2021). *Cytoskeleton*, **78**, 448–458.
Emsley, P., Lohkamp, B., Scott, W. G. & Cowtan, K. (2010). *Acta Cryst.* D**66**, 486–501.
Ge, J., Huang, F. & Nesmelov, Y. E. (2017). *Protein Sci.* **26**, 2181–2186.
Geeves, M. A. & Holmes, K. C. (1999). *Annu. Rev. Biochem.* **68**, 687–728.
Goodno, C. C. (1979). *Proc. Natl Acad. Sci. USA*, **76**, 2620–2624.
Goodno, C. C. (1982). *Methods Enzymol.* **85**, 116–123.
Houdusse, A., Szent-Györgyi, A. G. & Cohen, C. (2000). *Proc. Natl Acad. Sci. USA*, **97**, 11238–11243.
Huxley, H. E. (1969). *Science*, **164**, 1356–1366.
Klebl, D. P., McMillan, S. N., Risi, C., Forgacs, E., Virok, B., Atherton, J. L., Harris, S. A., Stofella, M., Winkelmann, D. A., Sobott, F., Galkin, V. E., Knight, P. J., Muench, S. P., Scarff, C. A. & White, H. D. (2025). *Nature*, **642**, 519–526.
Lewis, G. D., Voors, A. A., Cohen-Solal, A., Metra, M., Whellan, D. J., Ezekowitz, J. A., Böhm, M., Teerlink, J. R., Docherty, K. F., Lopes, R. D., Divanji, P. H., Heitner, S. B., Kupfer, S., Malik, F. I., Meng, L., Wohltman, A. & Felker, G. M. (2022). *JAMA*, **328**, 259–269.
Liebschner, D., Afonine, P. V., Baker, M. L., Bunkóczi, G., Chen, V. B., Croll, T. I., Hintze, B., Hung, L.-W., Jain, S., McCoy, A. J., Moriarty, N. W., Oeffner, R. D., Poon, B. K., Prisant, M. G., Read, R. J., Richardson, J. S., Richardson, D. C., Sammito, M. D., Sobolev, O. V., Stockwell, D. H., Terwilliger, T. C., Urzhumtsev, A. G., Videau, L. L., Williams, C. J. & Adams, P. D. (2019). *Acta Cryst.* D**75**, 861–877.
Liu, Y., White, H. D., Belknap, B., Winkelmann, D. A. & Forgacs, E. (2015). *Biochemistry*, **54**, 1963–1975.
Malik, F. I., Hartman, J. J., Elias, K. A., Morgan, B. P., Rodriguez, H., Brejc, K., Anderson, R. L., Sueoka, S. H., Lee, K. H., Finer, J. T., Sakowicz, R., Baliga, R., Cox, D. R., Garard, M., Godinez, G., Kawas, R., Kraynack, E., Lenzi, D., Lu, P. P., Muci, A., Niu, C., Qian, X., Pierce, D. W., Pokrovskii, M., Suehiro, I., Sylvester, S., Tochimoto, T., Valdez, C., Wang, W., Katori, T., Kass, D. A., Shen, Y.-T., Vatner, S. F. & Morgans, D. J. (2011). *Science*, **331**, 1439–1443.
McMillan, S. N., Pitts, J. R. T., Barua, B., Winkelmann, D. A. & Scarff, C. A. (2026). *Sci. Adv.* **12**, eaea9335.
Moretto, L., Ušaj, M., Matusovsky, O., Rassier, D. E., Friedman, R. & Månsson, A. (2022). *Nat. Commun.* **13**, 4575.
Morgan, B. P., Muci, A., Lu, P.-P., Qian, X., Tochimoto, T., Smith, W. W., Garard, M., Kraynack, E., Collibee, S., Suehiro, I., Tomasi, A., Valdez, S. C., Wang, W., Jiang, H., Hartman, J., Rodriguez, H. M., Kawas, R., Sylvester, S., Elias, K. A., Godinez, G., Lee, K., Anderson, R., Sueoka, S., Xu, D., Wang, Z., Djordjevic, N., Malik, F. I. & Morgans, D. J. Jr (2010). *ACS Med. Chem. Lett.* **1**, 472–477.
Muretta, J. M., Rohde, J. A., Johnsrud, D. O., Cornea, S. & Thomas, D. D. (2015). *Proc. Natl Acad. Sci. USA*, **112**, 14272–14277.
Nagy, L., Kovács, Á., Bódi, B., Pásztor, E. T., Fülöp, G., Tóth, A., Édes, I. & Papp, Z. (2015). *Br. J. Pharmacol.* **172**, 4506–4518.

Pettersen, E. F., Goddard, T. D., Huang, C. C., Meng, E. C., Couch, G. S., Croll, T. I., Morris, J. H. & Ferrin, T. E. (2021). *Protein Sci.* **30**, 70–82.
Planelles-Herrero, V. J., Hartman, J. J., Robert-Paganin, J., Malik, F. I. & Houdusse, A. (2017). *Nat. Commun.* **8**, 190.
Punjani, A., Rubinstein, J. L., Fleet, D. J. & Brubaker, M. A. (2017). *Nat. Methods*, **14**, 290–296.
Punjani, A., Zhang, H. & Fleet, D. J. (2020). *Nat. Methods*, **17**, 1214–1221.
Robert-Paganin, J., Pylypenko, O., Kikuti, C., Sweeney, H. L. & Houdusse, A. (2020). *Chem. Rev.* **120**, 5–35.
Smith, C. A. & Rayment, I. (1996). *Biochemistry*, **35**, 5404–5417.
Teerlink, J. R., Diaz, R., Felker, G. M., McMurray, J. J. V., Metra, M., Solomon, S. D., Adams, K. F., Anand, I., Arias-Mendoza, A., Biering-Sørensen, T., Böhm, M., Bonderman, D., Cleland, J. G. F., Corbalan, R., Crespo-Leiro, M. G., Dahlström, U., Echeverria, L. E., Fang, J. C., Filippatos, G., Fonseca, C., Goncalvesova, E., Goudev, A. R., Howlett, J. G., Lanfear, D. E., Li, J., Lund, M., Macdonald, P., Mareev, V., Momomura, S., O'Meara, E., Parkhomenko, A., Ponikowski, P., Ramires, F. J. A., Serpytis, P., Sliwa, K., Spinar, J., Suter, T. M., Tomcsanyi, J., Vandekerckhove, H., Vinereanu, D., Voors, A. A., Yilmaz, M. B., Zannad, F., Sharpsten, L., Legg, J. C., Varin, C., Honarpour, N., Abbasi, S. A., Malik, F. I. & Kurtz, C. E. (2021). *N. Engl. J. Med.* **384**, 105–116.
Wilson, G. J., Shull, S. E. & Cooke, R. (1995). *Biophys. J.* **68**, 216–226.
Woody, M. S., Greenberg, M. J., Barua, B., Winkelmann, D. A., Goldman, Y. E. & Ostap, E. M. (2018). *Nat. Commun.* **9**, 3838.
Woody, M. S., Winkelmann, D. A., Capitanio, M., Ostap, E. M. & Goldman, Y. E. (2019). *eLife*, **8**, e49266.